Zhang et al. Nanoscale Research Letters (2020) 15:32
https://doi.org/10.1186/s11671-020-3268-4

Nanoscale Research Letters

NANO EXPRESS Open Access

$CuFe_2O_4/MoS_2$ Mixed-Dimensional Heterostructures with Improved Gas Sensing Response

Kenan Zhang[1*], Changchun Ding[1], Yihong She[1], Zhen Wu[1], Changhui Zhao[2*], Baojun Pan[3], Lijie Zhang[3], Wei Zhou[4] and Qunchao Fan[1*]

Abstract

Mixed-dimensional (2D + *n*D, *n* = 0, 1, and 3) heterostructures opened up a new avenue for fundamental physics studies and applied nanodevice designs. Herein, a novel type-II staggered band alignment $CuFe_2O_4/MoS_2$ mixed-dimensional heterostructures (MHs) that present a distinct enhanced (20–28%) acetone gas sensing response compared with pure $CuFe_2O_4$ nanotubes are reported. Based on the structural characterizations and DFT calculation results, the tentative mechanism for the improvement of gas sensing performance of the $CuFe_2O_4/MoS_2$ MHs can be attributed to the synergic effect of type-II band alignment and the MoS_2 active sites.

Keywords: MoS_2, $CuFe_2O_4$ nanotubes, Heterostructures, First-principles calculations, Gas sensors

Introduction

Integration of nanostructured materials with dissimilar physical properties is essential for creating multifunctional devices and it has long been a pursuit of nanomaterials science community [1–5]. Two-dimensional (2D) layered materials, such as graphene, g-C_3N_4, and MoS_2, have received broad interdisciplinary attention [6–13], owing to their potential in diverse technologies, including sensors, electronics, optoelectronics, and so on [14–20]. In particular, 2D layered materials provide a new platform for building mixed-dimensional heterostructures (MHs) efficiently with 0D and 1D nanostructures (including quantum dots, nanowires, and nanotubes) [21–29]. According to previous reports, the electrical conductivity, surface activity, and sensing response of MHs can be efficiently tailored by choosing the suitable candidate materials [30–35]. Although most research has been focused on the novel physical properties of MHs based on 2D layered materials, more efforts are still needed to develop the 0D/1D MH-based nanodevices. $CuFe_2O_4$ is an important n-type metal oxide semiconductor with an indirect bandgap in the range of 1.3–1.95 eV [36, 37], which has been considered a promising material for gas sensors because of its naturally abundance, low-cost, environmental friendliness, simple electronic interface, low maintenance, ease of use, and fabrication [38–40]. It is worth noting that the $CuFe_2O_4$-based gas sensors exhibited relatively low responses toward some target gasses (such as ethanol and acetone) [37]. Therefore, it is significant to improve the sensitivity performance of $CuFe_2O_4$-based gas sensors by the reasonable design of MHs. MoS_2 is one of the most prominent 2D materials possessing a bandgap of 1.2–1.8 eV, because of high surface to volume ratio and highly sensitive to oxygen adsorption allowing their exploration in chemical sensing applications [41].

In this paper, we report a $CuFe_2O_4/MoS_2$ MHs (1D/2D) for the first time synthesized by two-step method using electrospinning followed by a hydrothermal process. The morphologies, crystal structures, and compositions of the $CuFe_2O_4/MoS_2$ MHs have been confirmed, and the density function theory (DFT) results further indicate the formation of type-II band alignment in the MHs. The $CuFe_2O_4/MoS_2$ MHs have obvious advantages for gas sensing, which benefits from the type-II band alignment and active sites in MoS_2 ultrathin

* Correspondence: knzhang@mail.sitp.ac.cn; zhaoch@sustech.edu.cn; fanqunchao@mail.xhu.edu.cn
[1]School of Science, Key Laboratory of High Performance Scientific Computation, Xihua University, Chengdu 610039, China
[2]School of Microelectronics, Southern University of Science and Technology, Shenzhen 518055, China
Full list of author information is available at the end of the article

nanosheets. Gas sensing properties of the $CuFe_2O_4/MoS_2$ MHs are studied in both ethanol and acetone gasses. As was expected, the MHs-based sensor shows substantial improved gas sensing performance compared with pure $CuFe_2O_4$ nanotubes therefore suggesting potential applications of $CuFe_2O_4/MoS_2$ MHs in highly sensitive gas sensors.

Method Section

Synthesis of $CuFe_2O_4/MoS_2$ MHs

The detailed preparation processes of $CuFe_2O_4/MoS_2$ MHs are shown in Fig. 1. Firstly, the pure $CuFe_2O_4$ nanotubes were pre-synthesized by electrospinning method. Firstly, 0.5 mmol of $Cu(NO_3)_2{\cdot}3H_2O$, 1.0 mmol of $Fe(NO_3)_3{\cdot}9H_2O$, and 0.68 g of polyvinylpyrrolidone (PVP) were dissolved in 5 mL of ethanol and 5 mL of N, N-Dimethylformamide(DMF). After stirring for 6 h, the above solution was placed in a syringe and injected with a feeding rate of 0.4 mL h^{-1}. A DC voltage of 15 kV was applied between the needle tip and stainless-steel mesh with a distance of 18 cm. The as-spun precursor fibers were collected in a tube furnace and maintained at 500 °C for 2 h in air.

The $CuFe_2O_4/MoS_2$ MHs were synthesized by hydrothermal method in the second step. $CuFe_2O_4$ nanotubes were dispersed in deionized (DI) water (15 mL) via sonication. The $(NH_4)_6Mo_7O_{24}{\cdot}4H_2O$ and CN_2H_4S were then added into the mixture. After stirring for 30 min, the solution was transferred into a 25-mL polytetrafluoroethylene (PTFE) autoclave and kept at 200 °C for 10 h. Finally, the MHs were collected in a centrifuge, washed with DI water and dried at 60 °C.

Microstructural Characterization

The morphology and structure of pure $CuFe_2O_4$ nanotubes and $CuFe_2O_4/MoS_2$ MHs were characterized by field emission scanning electron microscopy (FE-SEM, FEI NanoSEM200). X-ray diffraction (XRD) patterns were recorded on a Rigaku Smartlab with Cu Kα radiation operating at 45 kV and 200 mA. Transmission electron microscopy (TEM) measurements were conducted on the JEOL 2100F. The energy dispersive X-ray spectrometer (EDS) was introduced to identify the chemical composition. Raman measurements were performed using a Renishaw inVia at room temperature with a 532-nm excitation laser (2 mW).

Fabrication and Measurement of Gas Sensors

Gas sensors were fabricated by coating the mixture of the tested materials (pure $CuFe_2O_4$ or $CuFe_2O_4/MoS_2$ MHs) and DI water onto the interdigitated Au electrode arrays (gap and width are 200 μm) on the SiO_2/Si substrate. Gas sensing properties of the sensors were measured by using a commercial CGS-4TPs system (Beijing Elite Tech Co., Ltd., China). The response is defined as

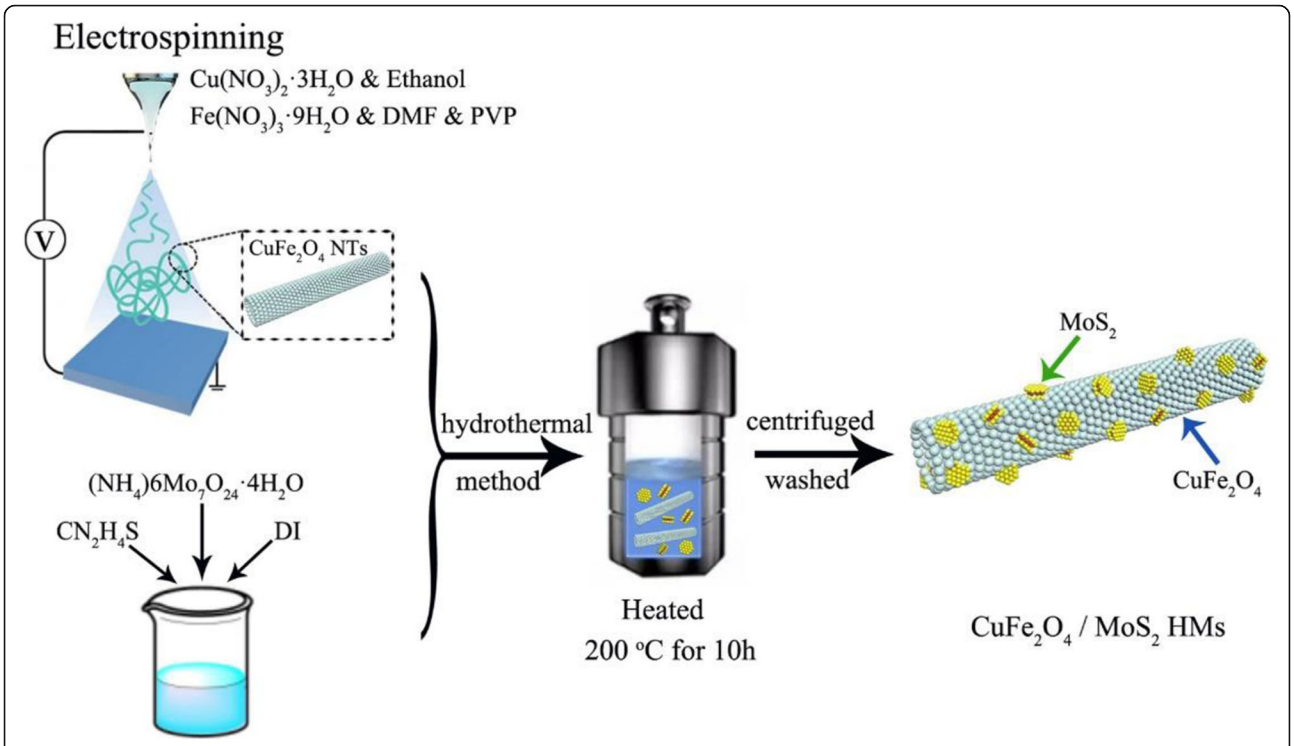

Fig. 1 Schematic illustration of the preparation processes of $CuFe_2O_4/MoS_2$ MHs

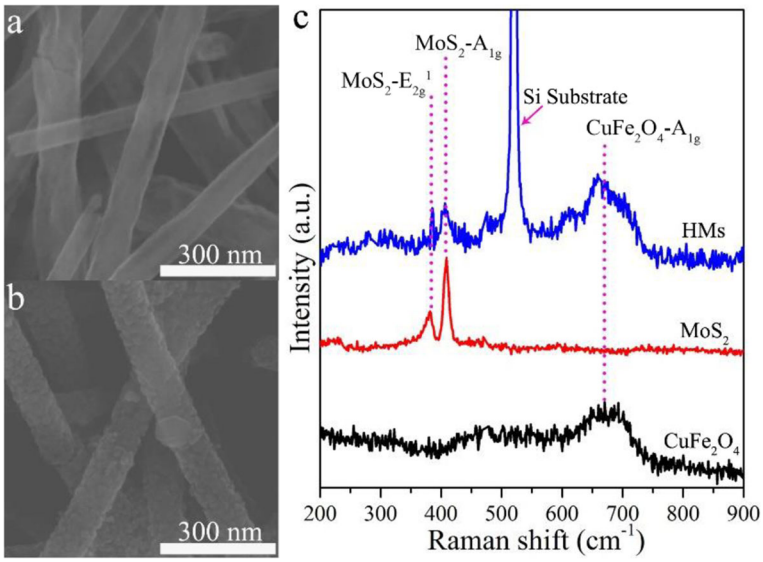

Fig. 2 SEM and Raman characterization of $CuFe_2O_4$ and $CuFe_2O_4/MoS_2$ MHs. FE-SEM images of **a** pure $CuFe_2O_4$ nanotubes and **b** $CuFe_2O_4/MoS_2$ MHs. **c** Raman spectra of pure $CuFe_2O_4$ nanotubes, pure MoS_2 nanosheets, and $CuFe_2O_4/MoS_2$ MHs

R_a/R_g, where R_a is the resistance in atmospheric air and R_g is the resistance in the tested gas, respectively.

Results and Discussion

The morphologies of pure $CuFe_2O_4$ nanotubes and $CuFe_2O_4/MoS_2$ MHs are shown in Fig. 2 and Additional file 1: Figure S1. Both of the samples are well-defined tubular nanostructures with several tens of micrometers in length, and 70–150 nm in diameter, which can be confirmed by the cross-section of broken nanotubes (Additional file 1: Figure S1b). The SEM images (Fig. 2a, b) show $CuFe_2O_4/MoS_2$ MHs still maintains the original tubular structure after the hydrothermal process. And we can see that the $CuFe_2O_4$ nanotubes have a relative smooth surface before compositing with tiny MoS_2, while the rough surfaces appear in the $CuFe_2O_4/MoS_2$ MHs. Moreover, Raman spectroscopies were performed to verify the presence of MoS_2 in the $CuFe_2O_4/MoS_2$ MHs. The strong vibrational modes of $CuFe_2O_4$ (T_{2g} – 477 cm^{-1}, A_{1g} – 685 cm^{-1}) and MoS_2 (E^1_{2g} – 382 cm^{-1}, A_{1g} – 409 cm^{-1}) can be found in pure $CuFe_2O_4$ nanotube or MoS_2 nanosheet samples (Fig. 2c). By comparing with the pure $CuFe_2O_4$ nanotubes and MoS_2 nanosheets (Additional file 1: Figure S2), the Raman vibrational mode of $CuFe_2O_4$ (T_{2g}, A_{1g}), and MoS_2 (E^1_{2g}, A_{1g}) all appeared in the Raman spectrum of $CuFe_2O_4/MoS_2$ MHs. The position of these four peaks is unchanged, indicating the formation of the composite structure of $CuFe_2O_4$ and MoS_2 in the $CuFe_2O_4/MoS_2$ MHs. Meanwhile, the XRD results of pure $CuFe_2O_4$ and $CuFe_2O_4/MoS_2$ MHs are shows in Additional file 1: Figure S3. It can be seen that the diffraction peaks of $CuFe_2O_4$ are well indexed to the standard JCPDS card (34-0425), revealing that the $CuFe_2O_4$ belongs to a body-centered tetragonal structure. The XRD pattern of the $CuFe_2O_4/MoS_2$ is superimposed by the diffraction peaks of $CuFe_2O_4$ and MoS_2,

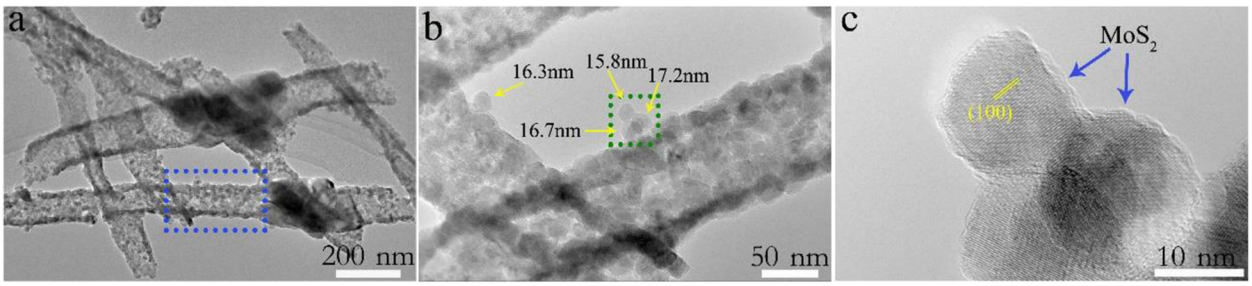

Fig. 3 TEM characterization of $CuFe_2O_4/MoS_2$ MHs. Low-resolution TEM image of **a** $CuFe_2O_4/MoS_2$ MHs and **b** partial zooming panel **a** in the dotted line. **c** HRTEM image of the region in the dotted line in the **b**

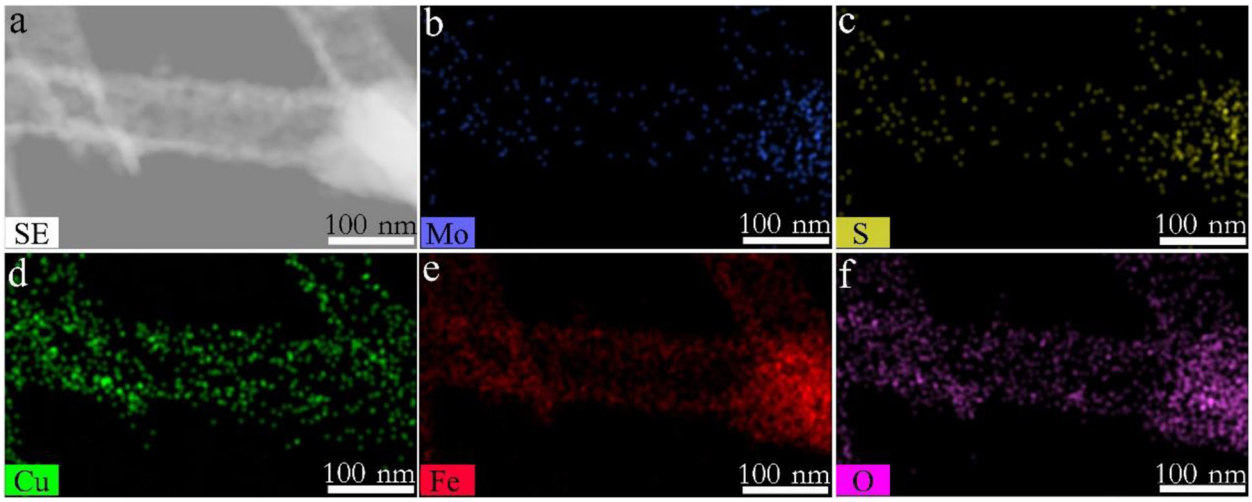

Fig. 4 EDS result of $CuFe_2O_4/MoS_2$ MHs. **a** SEM image of sample in dotted line of Fig. 3a. **b**–**f** The in-suit EDS intensity map of Mo, S, Cu, Fe, and O, respectively

respectively (the standard JCPDS card of $CuFe_2O_4$ (34-0425) and MoS_2 (06-0097)), and there is no characteristic peak for impurity in the XRD pattern, indicating that the composite is consisted by the $CuFe_2O_4$ and MoS_2 only.

To further characterize the microstructure of $CuFe_2O_4/MoS_2$ MHs, TEM observations were carried out, as shown in Fig. 3 a. The low-resolution TEM images (Fig. 3b) show that the surfaces of $CuFe_2O_4$ nanotubes are uniformly covered with many hexagonal nanosheets 15–20 nm in diameter. Figure 3 c gives the high-resolution TEM (HRTEM) images of tiny nanosheets marked in Fig. 3b. The lattice fringes spacing of 0.27 nm can be corresponded to the (100) plane of MoS_2. In addition, the morphology and size of MoS_2 can be tailored by adjusting the hydrothermal reaction conditions (Additional file 1: Figure S2). Selected area electron diffraction (SAED) pattern also reveals the hexagonal symmetry for the layered MoS_2 (Additional file 1: Figure S4). To demonstrate the

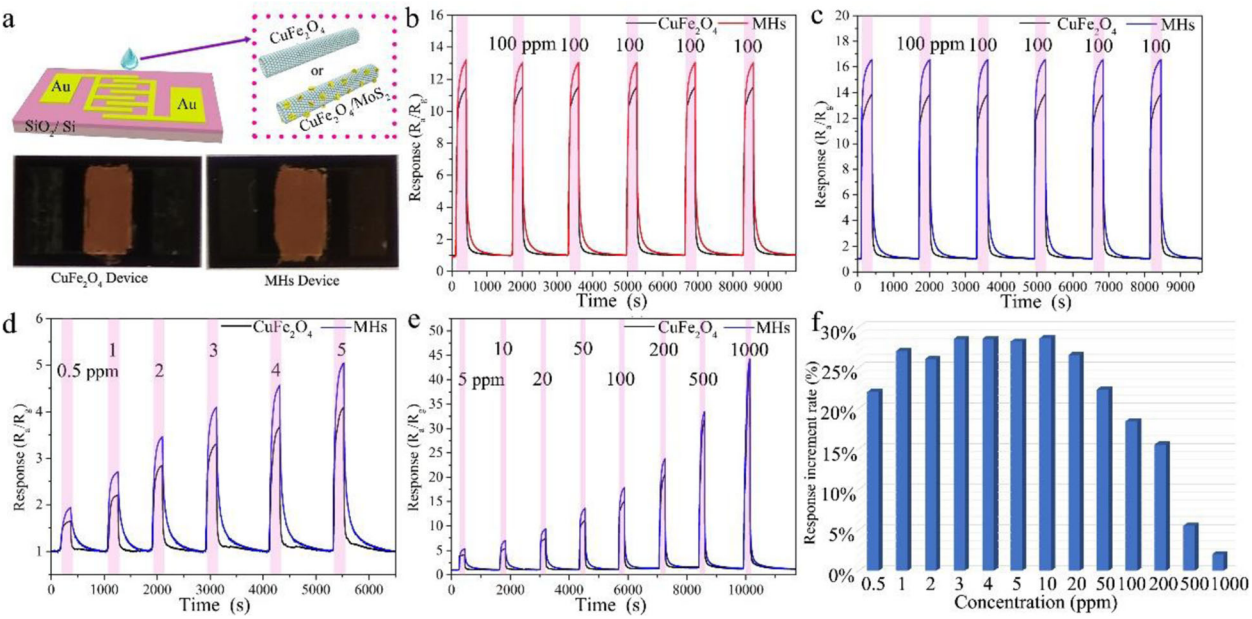

Fig. 5 Sensing measurements of $CuFe_2O_4/MoS_2$ MHs. **a** Fabricated diagram of gas sensor and photos of fabricated gas sensor ($CuFe_2O_4$ nanotubes and $CuFe_2O_4/MoS_2$ MHs). Sensing reproducibility of the $CuFe_2O_4$ nanotubes and $CuFe_2O_4/MoS_2$ MHs gas sensor to 100 ppm **b** ethanol and **c** acetone. **d**, **e** Dynamic response-recovery curves of $CuFe_2O_4$ nanotubes and $CuFe_2O_4/MoS_2$ MHs gas sensors at different acetone concentrations. **f** The response increment rate of $CuFe_2O_4/MoS_2$ MHs device relative to pure $CuFe_2O_4$ nanotube device at different acetone concentrations

distribution of MoS_2 nanosheets on the surface of $CuFe_2O_4$ nanotubes, the in situ EDS elemental mapping images of $CuFe_2O_4/MoS_2$ MHs (marked in Fig. 3b) are performed as shown in Fig. 4. The homogeneous distribution of Mo, S, Cu, Fe, and O elements indicates that a large number of MoS_2 nanosheets are uniformly dispersed in $CuFe_2O_4/MoS_2$ MHs.

In order to investigate their gas sensing properties, the pure $CuFe_2O_4$ nanotubes and $CuFe_2O_4/MoS_2$ MHs gas sensors were fabricated as shown in Fig. 5 a and Additional file 1: Figure S5. Figure 5b and c preset the response-recovery curves of pure $CuFe_2O_4$ nanotubes and $CuFe_2O_4/MoS_2$ MHs gas sensors toward 100 ppm ethanol and acetone (6 cycles), respectively. After compositing with the MoS_2 nanosheets, it can be seen that the $CuFe_2O_4/MoS_2$ MHs sensor shows positive responses on exposure to both ethanol and acetone, which are about 18–20% higher than those of pure $CuFe_2O_4$ nanotubes. Evidently, the $CuFe_2O_4/MoS_2$ MHs sensor exhibits consistent sensing responses even after 6 cycles, indicating the good reversibility and repeatability. Figure 5d and e give the dynamic transient response curves of pure $CuFe_2O_4$ nanotubes and $CuFe_2O_4/MoS_2$ MHs gas sensors to various acetone concentrations (0.5–1000 ppm). The $CuFe_2O_4/MoS_2$ MHs sensor exhibits improved response to each acetone concentration (Fig. 5f). In particular, the percentage of improvement in acetone response exceeds 20% at acetone concentrations not higher than 50 ppm. It is noticeable that the acetone responses improved about 18% even at 0.5 ppm. That means the $CuFe_2O_4/MoS_2$ MHs are more sensitive to acetone in contrast with pure $CuFe_2O_4$.

To probe the important role of MoS_2 nanosheets in the gas sensing reaction, the electronic band structures of $CuFe_2O_4$ and multilayer MoS_2 were calculated respectively by using DFT (Fig. 6a, b). The indirect bandgap of $CuFe_2O_4$ and multilayer MoS_2 is about 1.3 eV and 1.2 eV, respectively. According to the results, the band alignment of $CuFe_2O_4/MoS_2$ MHs is drawn in Fig. 6c, which forms a type-II band alignment. The improvement of sensor response manifested in changes in the electrical resistance (R_a/R_g) in the presence of air or target gas. Because of the type-II band alignment, the electron-hole pairs can be separated effectively at the heterojunction

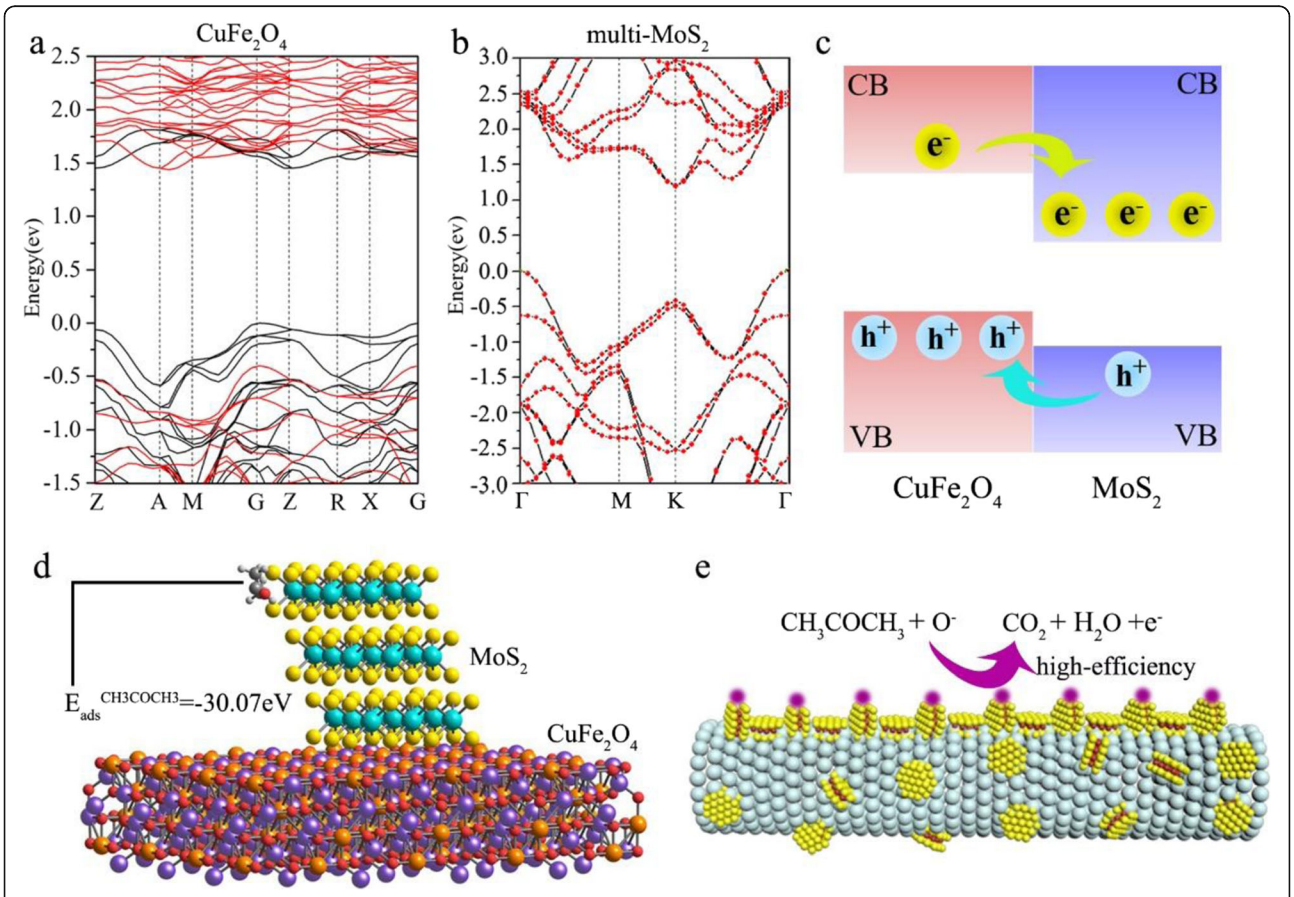

Fig. 6 DFT results of $CuFe_2O_4/MoS_2$ MHs. Electronic structures of **a** $CuFe_2O_4$ nanotubes and **b** multilayer MoS_2. **c** Schematic illustrations of the type-II band alignment in $CuFe_2O_4/MoS_2$ MHs. **d** The edge adsorption energy for CH_3COCH_3 molecules on $CuFe_2O_4/MoS_2$ MHs. **e** Model for the $CuFe_2O_4/MoS_2$ MHs in acetone vapor

interface. Holes remain within the $CuFe_2O_4$ nanotubes, while most electrons will be injected into MoS_2 layers. When the pure $CuFe_2O_4$ or $CuFe_2O_4/MoS_2$ MHs sensors are exposed to air, oxygen molecules will adsorb on the surface of sensors to generate oxygen species (O_2^-, O^-, and O^{2-}). Meanwhile, the free electrons transfer from $CuFe_2O_4$ or $CuFe_2O_4/MoS_2$ MHs to oxygen species at sensors surface lead to the decreases of electrical resistance (R_a). In the case of target gas detection, the reaction of adsorbed oxygen species and target molecules will occur on the sensor surface (e.g., $CH_3COCH_3 + 8O^- \rightarrow 3CO_2 + 3H_2O + 8e^-$) and release free electrons to the $CuFe_2O_4$ or $CuFe_2O_4/MoS_2$ MHs. Thus, the sensor resistance (R_g) decreases in target gas. It is noteworthy that the MoS_2 edges offer high density of potential active sites for reduction reaction [42–44]. Figure 6 d shows the calculated adsorption energy of CH_3COCH_3 on $CuFe_2O_4/MoS_2$ MHs by using the DFT method. The adsorption energy for CH_3COCH_3 molecules over the edge of $CuFe_2O_4/MoS_2$ MHs is − 30.07 eV (very small). That means the edge of $CuFe_2O_4/MoS_2$ MHs are active sites for CH_3COCH_3 molecules. Benefiting from the active sites in MoS_2 nanosheets, the $CuFe_2O_4/MoS_2$ MHs obtained free electrons more efficiently compared with pure $CuFe_2O_4$ (Fig. 6e). The positive effect is more obvious in low target gas concentration. While the improved gas response performance is limited in the extra-high concentrations due to the limited active sites.

Conclusions

We report a novel $CuFe_2O_4/MoS_2$ MHs and the obvious improvement of sensing performance for acetone. The $CuFe_2O_4/MoS_2$ MHs are confirmed by Raman, SEM, XRD, TEM, and EDS results. The coupling interactions between $CuFe_2O_4$ and MoS_2 lead to the formation of type-II heterostructures, which is verified by DFT results. The practical gas sensor devices were fabricated based on $CuFe_2O_4/MoS_2$ MHs and shows the high sensitivity and excellent repeatability. A sensing enhancement is also seen with ethanol gas. The enhancement of gas sensing properties of the $CuFe_2O_4/MoS_2$ MHs can be attributed to the effect of type-II band alignment and the MoS_2 active sites. We believe that our studies will be valuable for the various applications of mixed-dimensional heterostructures.

Supplementary information

Supplementary information accompanies this paper at https://doi.org/10.1186/s11671-020-3268-4.

Additional file 1: Figures S1–S5. Additional experimental details, SEM, TEM, SAED and XRD results.

Abbreviations

2D: Two-dimensional; DFT: Density function theory; EDS: Energy dispersive X-ray spectrometer; MHs: Mixed-dimensional heterostructures; SEM: Scanning electron microscope; TEM: Transmission electron microscopy

Authors' Contributions

KNZ, CHZ, CCD, and QCF performed the experimental design and analysis and wrote the manuscript. CCD, ZW, and BJP contributed to the preparation of devices and TEM and SEM measurements. YHS, LJZ, and WZ contributed to the Raman spectroscopy and sensing measurements. KNZ and CCD contributed equally to this work. All authors read and approved the final manuscript.

Funding

This work was funded by the Department of Science and Technology of Sichuan Province (2019YFG0446) and Sichuan Distinguished Scientists of China (grant no. 2019JDJQ0050).

Availability of Data and Materials

All data are fully available without restriction.

Competing Interests

The authors declare that they have no competing interests.

Author details

[1]School of Science, Key Laboratory of High Performance Scientific Computation, Xihua University, Chengdu 610039, China. [2]School of Microelectronics, Southern University of Science and Technology, Shenzhen 518055, China. [3]Zhejiang Key Laboratory of Carbon Materials, College of Chemistry and Materials Engineering, Wenzhou University, Wenzhou 325035, China. [4]National Laboratory for Infrared Physics, Shanghai Institute of Technical Physics, Chinese Academy of Sciences, Shanghai 200083, China.

Received: 16 October 2019 Accepted: 27 January 2020
Published online: 03 February 2020

References

1. Liu Y, Huang Y, Duan X (2019) Van der Waals integration before and beyond two-dimensional materials. Nature 567:323–333
2. Sahoo PK, Memaran S, Xin Y, Balicas L, Gutiérrez HR (2018) One-pot growth of two-dimensional lateral heterostructures via sequential edge-epitaxy. Nature 553:63
3. Jariwala D, Marks TJ, Hersam MC (2016) Mixed-dimensional van der Waals heterostructures. Nat Mater 16:170
4. Unuchek D, Ciarrocchi A, Avsar A, Watanabe K, Taniguchi T, Kis A (2018) Room-temperature electrical control of exciton flux in a van der Waals heterostructure. Nature 560:340–344
5. Dong H, Xu F, Sun Z, Wu X, Zhang Q, Zhai Y, Tan XD, He L, Xu T, Zhang Z, Duan X, Sun L (2019) In situ interface engineering for probing the limit of quantum dot photovoltaic devices. Nat Nanotechnol 14:950–956
6. Klein J, Lorke M, Florian M, Sigger F, Sigl L, Rey S, Wierzbowski J, Cerne J, Müller K, Mitterreiter E, Zimmermann P, Taniguchi T, Watanabe K, Wurstbauer U, Kaniber M, Knap M, Schmidt R, Finley JJ, Holleitner AW (2019) Site-selectively generated photon emitters in monolayer MoS_2 via local helium ion irradiation. Nat Commun 10:2755
7. Shivayogimath A, Thomsen JD, Mackenzie DMA, Geisler M, Stan R-M, Holt AJ, Bianchi M, Crovetto A, Whelan PR, Carvalho A, Neto AHC, Hofmann P, Stenger N, Bøggild P, Booth TJ (2019) A universal approach for the synthesis of two-dimensional binary compounds. Nat Commun 10:2957
8. Rhodes D, Chae SH, Ribeiro-Palau R, Hone J (2019) Disorder in van der Waals heterostructures of 2D materials. Nat Mater 18:541–549
9. Zhang K, Hu S, Zhang Y, Zhang T, Zhou X, Sun Y, Li T-X, Fan HJ, Shen G, Chen X, Dai N (2015) Self-induced uniaxial strain in MoS2 monolayers with local van der Waals-stacked interlayer interactions. ACS Nano 9:2704–2710
10. Fang Y, Hu X, Zhao W, Pan J, Wang D, Bu K, Mao Y, Chu S, Liu P, Zhai T, Huang F (2019) Structural determination and nonlinear optical properties of new 1T‴-type MoS2 compound. J Am Chem Soc 141:790–793
11. Hu F, Kim M, Zhang Y, Luan Y, Ho KM, Shi Y, Wang CZ, Wang X, Fei Z (2019) Tailored plasmons in pentacene/graphene heterostructures with interlayer electron transfer. Nano Lett 19:6058–6064

12. Ran J, Guo W, Wang H, Zhu B, Yu J, Qiao S-Z (2018) Metal-free 2D/2D Phosphorene/g-C3N4 van der Waals heterojunction for highly enhanced visible-light photocatalytic H2 production. Adv Mater 30:1800128
13. Fu J, Xu Q, Low J, Jiang C, Yu J (2019) Ultrathin 2D/2D WO3/g-C3N4 step-scheme H2-production photocatalyst. Appl Catal B Environ 243:556–565
14. Raja A, Waldecker L, Zipfel J, Cho Y, Brem S, Ziegler JD, Kulig M, Taniguchi T, Watanabe K, Malic E, Heinz TF, Berkelbach TC, Chernikov A (2019) Dielectric disorder in two-dimensional materials. Nature Nanotechnology 14:832–837
15. Lin Z, Liu Y, Halim U, Ding M, Liu Y, Wang Y, Jia C, Chen P, Duan X, Wang C, Song F, Li M, Wan C, Huang Y, Duan X (2018) Solution-processable 2D semiconductors for high-performance large-area electronics. Nature 562: 254–258
16. Lv L, Zhuge F, Xie F, Xiong X, Zhang Q, Zhang N, Huang Y, Zhai T (2019) Reconfigurable two-dimensional optoelectronic devices enabled by local ferroelectric polarization. Nat Commun 10:3331
17. Long M, Wang P, Fang H, Hu W (2019) Progress, challenges, and opportunities for 2D material based photodetectors. Adv Funct Mater 29:1803807
18. Cheng R, Wang F, Yin L, Wang Z, Wen Y, Shifa TA, He J (2018) High-performance, multifunctional devices based on asymmetric van der Waals heterostructures. Nat Elect 1:356–361
19. Wang X, Yu P, Lei Z, Zhu C, Cao X, Liu F, You L, Zeng Q, Deng Y, Zhou J, Fu Q, Wang J, Huang Y, Liu Z (2019) Van der Waals negative capacitance transistors. Nat Commun 10:3037
20. Chen X, Zhang J, Fu X, Antonietti M, Wang X (2009) Fe-g-C3N4-catalyzed oxidation of benzene to phenol using hydrogen peroxide and visible light. J Am Chem Soc 131:11658–11659
21. Zhang K, Chen W, Zhang L, Zhou W, Fan Q (2019) Atomically thin WSe2/CdSe mixed-dimensional van der Waals heterostructures with enhanced optoelectrical properties. ACS Photonics 6(8):2067–2072
22. Zhang K, Zhang T, Cheng G, Li T, Wang S, Wei W, Zhou X, Yu W, Sun Y, Wang P, Zhang D, Zeng C, Wang X, Hu W, Fan HJ, Shen G, Chen X, Duan X, Chang K, Dai N (2016) Interlayer transition and infrared photodetection in atomically thin type-II MoTe2/MoS2 van der Waals heterostructures. ACS Nano 10:3852–3858
23. Zhang K, Zhang Y, Zhang T, Dong W, Wei T, Sun Y, Chen X, Shen G, Dai N (2015) Vertically coupled ZnO nanorods on MoS2 monolayers with enhanced Raman and photoluminescence emission. Nano Res 8:743–750
24. Wang C, He Q, Halim U, Liu Y, Zhu E, Lin Z, Xiao H, Duan X, Feng Z, Cheng R, Weiss NO, Ye G, Huang Y-C, Wu H, Cheng H-C, Shakir I, Liao L, Chen X, Goddard Iii WA, Huang Y, Duan X (2018) Monolayer atomic crystal molecular superlattices. Nature 555:231
25. Lee YT, Jeon PJ, Han JH, Ahn J, Lee HS, Lim JY, Choi WK, Song JD, Park M-C, Im S, Hwang DK (2017) Mixed-dimensional 1D ZnO–2D WSe2 van der Waals heterojunction device for photosensors. Adv Funct Mater 27:1703822
26. Huang X, Tan C, Yin Z, Zhang H (2014) 25th anniversary article: hybrid nanostructures based on two-dimensional nanomaterials. Adv Mater 26: 2185–2204
27. Xiao Y, Zhang T, Zhou M, Weng Z, Chang X, Yang K, Liu J, Li J, Wei B, Wang Z, Fu L (2019) 2D material disassembly: disassembly of 2D vertical heterostructures. Adv Mater 31:1970022
28. Yuan L, Zhang C, Zhang X, Lou M, Ye F, Jacobson CR, Dong L, Zhou L, Lou M, Cheng Z, Ajayan PM, Nordlander P, Halas NJ (2019) Photocatalytic hydrogenation of graphene using Pd nanocones. Nano Lett 19:4413–4419
29. Zheng B, Zheng W, Jiang Y, Chen S, Li D, Ma C, Wang X, Huang W, Zhang X, Liu H, Jiang F, Li L, Zhuang X, Wang X, Pan A (2019) WO3–WS2 vertical bilayer heterostructures with high photoluminescence quantum yield. J Am Chem Soc 141:11754–11758
30. Geim AK, Grigorieva IV (2013) Van der Waals heterostructures. Nature 499:419
31. Novoselov KS, Mishchenko A, Carvalho A, Castro Neto AH (2016) 2D materials and van der Waals heterostructures. Science 353:9439
32. Liu Y, Weiss NO, Duan X, Cheng H-C, Huang Y, Duan X (2016) Van der Waals heterostructures and devices. Nat Rev Mater 1:16042
33. Wang L, Zou X, Lin J, Jiang J, Liu Y, Liu X, Zhao X, Liu YF, Ho JC, Liao L (2019) Perovskite/black ohosphorus/MoS2 photogate reversed photodiodes with ultrahigh light on/off ratio and fast response. ACS Nano 13:4804–4813
34. Konstantatos G, Badioli M, Gaudreau L, Osmond J, Bernechea M, de Arquer FPG, Gatti F, Koppens FHL (2012) Hybrid graphene–quantum dot phototransistors with ultrahigh gain. Nat Nanotechnol 7:363–368
35. Duan X, Wang C, Pan A, Yu R, Duan X (2015) Two-dimensional transition metal dichalcogenides as atomically thin semiconductors: opportunities and challenges. Chem Soc Rev 44:8859–8876
36. Park S, Baek JH, Zhang L, Lee JM, Stone KH, Cho IS, Guo J, Jung HS, Zheng X (2019) Rapid flame-annealed CuFe2O4 as efficient photocathode for photoelectrochemical hydrogen production. ACS Sust Chem Eng 7:5867–5874
37. Zhao C, Lan W, Gong H, Bai J, Ramachandran R, Liu S, Wang F (2018) Highly sensitive acetone-sensing properties of Pt-decorated CuFe2O4 nanotubes prepared by electrospinning. Ceramics Int 44:2856–2863
38. Šutka A, Gross KA (2016) Spinel ferrite oxide semiconductor gas sensors. Sensors Actuators B Chem 222:95–105
39. Li X, Liu A, Chu D, Zhang C, Du Y, Huang J, Yang P (2018) High performance of manganese porphyrin sensitized p-Type CuFe2O4 photocathode for solar water splitting to produce hydrogen in a tandem photoelectrochemical cell. Catalysts 8:108
40. Zhu M, Meng D, Wang C, Diao G (2013) Facile fabrication of hierarchically porous CuFe2O4 nanospheres with enhanced capacitance property. ACS Appl Mater Interfaces 5:6030–6037
41. Pham T, Li G, Bekyarova E, Itkis ME, Mulchandani A (2019) MoS_2 based optoelectronic gas sensor with sub parts per billion limit of NO_2 gas detection. ACS Nano 13:3196–3205
42. Jaramillo TF, Jørgensen KP, Bonde J, Nielsen JH, Horch S, Chorkendorff I (2007) Identification of active edge sites for electrochemical H2 evolution from MoS2 nanocatalysts. Science 317:100–102
43. Xie J, Zhang H, Li S, Wang R, Sun X, Zhou M, Zhou J, Lou XW, Xie Y (2013) Defect-rich MoS2 ultrathin nanosheets with additional active edge sites for enhanced electrocatalytic hydrogen evolution. Adv Mater 25:5807–5813
44. Chia X, Ambrosi A, Sofer Z, Luxa J, Pumera M (2015) Catalytic and charge transfer properties of transition metal dichalcogenides arising from electrochemical pretreatment. ACS Nano 9:5164–5179

Publisher's Note